Passive Nonreciprocity in a System of Asymmetrical Rotational Oscillators

Lezheng Fang, Alireza Mojahed, Amir Darabi, Alexander F. Vakakis, and Michael J. Leamy

Phys. Rev. Applied **15**, 034005 — Published 2 March 2021

DOI: 10.1103/PhysRevApplied.15.034005

Passive non-reciprocity in a system of asymmetrical rotational oscillators

Lezheng Fang[1], Alireza Mojahed[2], Amir Darabi[1, 2], Alexander F. Vakakis[2], Michael J. Leamy[1*]

[1] George W. Woodruff School of Engineering, Georgia Institute of Technology, Atlanta GA
lezheng.fang@gatech.edu, amirdarabi@gatech.edu, michael.leamy@me.gatech.edu
[2] Department of Mechanical Science and Engineering, University of Illinois at Urbana-Champaign, Champaign IL
mojahed2@illinois.edu, avakakis@illinois.edu
**Corresponding Author*

Abstract

In this paper we investigate an elastically-linked, nonlinear, in-plane rotator system and experimentally study its non-reciprocal impulse response. The nonlinearity of the system arises from the angled elastic linkage in rotational motion. A chain of rotators coupled with such linkages reaches an acoustic vacuum when the pretension of the elastic links vanish, leading to large nonlinearity tunable via small pretension. Using an analytical model and experimental exploration, we observe a broadband non-reciprocity in a weakly pre-tensioned, asymmetric, three-rotator system. In addition, we use a nonlinear normal mode (NNM) analysis, capturing the main qualitative dynamics of the response, to explain the observed non-reciprocity mechanism. The analysis shows that equal applied impulses, combined with energy-dependent frequency/mode shapes, result in robust non-reciprocity features, contrary to the reciprocal response present in the linear counterpart of this system.

1 Introduction

Reciprocity, a fundamental property of linear time-invariant systems, ensures an identical response when a source and receiver interchange position [1-3]. Breaking reciprocity, due to its large potential in applications such as targeted energy transfer [4-8], wave transmission control [9-17],

[1] Address all correspondence to this author.

and signal filtering/protection [18-20], has attracted increased recent attention. In acoustic and elastic media, *active* means to break reciprocity have adopted odd-symmetry field/circulation [12,15,21], time modulated materials [13,18,22-26] and external control [27-29], as reviewed in [30]. However, these active methods, due to their complexity and external dependencies, raise concerns about instability and energy consumption for practical implementation [27].

An alternative for achieving non-reciprocity relies on nonlinear mechanisms and system asymmetry, which can be realized in a *passive* manner and thus avoid the aforementioned shortcomings of active systems. In general, a nonlinear system may not break reciprocity or behave in a non-reciprocal fashion, particularly when the system's symmetry is maintained. Li *et al.* leveraged nonlinearity-induced higher harmonics to bypass the bandgap of a superlattice in one direction [10,11]. Other researchers utilized nonlinear bifurcations in a variety of systems to break reciprocity [5,28,31,32]. In phononic structures, nonlinear propagation zones in both weakly and strongly nonlinear lattices exhibit direction dependency due to asymmetry, leading to tunable non-reciprocity [19,33-36]. In low degree of freedom nonlinear systems, a new non-reciprocity mechanism has been identified which occurs due to nonlinear resonance and targeted energy transfer [6]. However, this mechanism requires symmetry breaking by a boundary nonlinear energy sink, which needs to be ungrounded and free to oscillate from one end of the lattice, restricting its generality.

Inspired by [6,37,38], in this paper we propose an asymmetric, lightly pre-tensioned, three-rotator system exhibiting passive non-reciprocity due to strong geometric nonlinearity. We show that the geometric nonlinearity in the system is tunable to the pretension of the elastic couplings, whose

absence leads to an acoustic vacuum [37,39]. Using this system, we uncover a new, broadly-applicable passive mechanism that passively breaks acoustic reciprocity. The simple three-rotator system exhibits broadband non-reciprocity in experimental tests, which agrees well with results from direct numerical simulation of an associated analytical model. Unlike non-reciprocity mechanisms featuring nonlinear resonance or bifurcation, we show that the observed non-reciprocal response arises from energy-dependent nonlinear normal modes (NNMs) intrinsic to the unit cell. Further, interpreting nonlinear non-reciprocity using NNM analysis suggests a new tool for exploring non-reciprocity in nonlinear media, which can be extrapolated to a class of nonlinear non-reciprocal problems where excitations induce distinct energies.

2 System Description

Figure 1a depicts three in-plane rotators linked by linear springs at their arms. Each rotator, with identical arm length, is pinned at its center and allows only rotational motion. The massless spring deforms only in its axial direction. The system is scaled by a moment of inertia hierarchy $I_1 < I_2 < I_3$. In this paper, we only consider small-angle oscillations around the equilibrium under

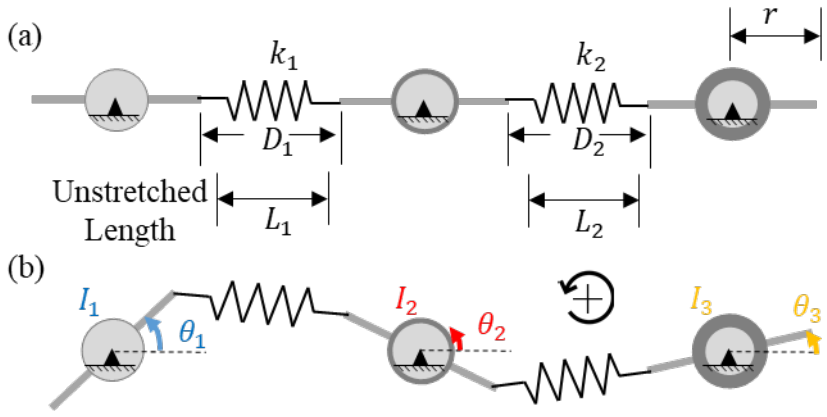

Figure 1: System Description. (a) Depiction of three in-plane rotators at the equilibrium position with system parameters marked. (b) Depiction at arbitrary angular displacement indicating the angular measures and spring stretch.

the condition $L_i \le D_i$ (i.e., each spring is either pre-tensioned or un-stretched at the position shown in Fig. 1a). Further, we define the angular displacement for these rotators counter-clockwise positive, as shown in Fig. 1b.

We next present the rotators' equations of motion. Each rotator is subject to a restoring and dissipation torque,

$$I_1 \ddot{\boldsymbol{\theta}}_1 - \boldsymbol{T}_{1,2} - \boldsymbol{T}_1 = 0 \tag{1}$$

$$I_2 \ddot{\boldsymbol{\theta}}_2 - \boldsymbol{T}_{2,1} - \boldsymbol{T}_{2,3} - \boldsymbol{T}_2 = 0 \tag{2}$$

$$I_3 \ddot{\boldsymbol{\theta}}_3 - \boldsymbol{T}_{3,2} - \boldsymbol{T}_3 = 0, \tag{3}$$

where $\boldsymbol{T}_{i,j}$ describes the restoring torque on the rotator resulting from the elastic linkage between the i^{th} and j^{th} rotators, and $\boldsymbol{T}_i$ denotes the equivalent dissipation torque on the i^{th} rotator. Due to the rotation, the rotator arm stretches the elastic linkage along an angle, and the restoring torque becomes non-proportional to the elastic linkage deformation. We derive the restoring torque from the rotation geometry,

$$\boldsymbol{r_i} = r\cos\left(\theta_i\right) i + r\sin\left(\theta_i\right) j \tag{4}$$

$$\boldsymbol{r_j} = r\cos\left(\theta_j\right) i + r\sin\left(\theta_j\right) j \tag{5}$$

$$L = \left(2r + D_{i^*}\right) i - \boldsymbol{r}_1 - \boldsymbol{r}_2 \tag{6}$$

$$\Delta L = \left|\boldsymbol{L}\right| - L_{i^*} \tag{7}$$

$$\boldsymbol{T}_{i,j} = \boldsymbol{r}_i \times \left(k_{i^*} \Delta L \frac{\boldsymbol{L}}{|\boldsymbol{L}|} \right), \tag{8}$$

where i, j denotes the indices of two adjacent rotators, and $i^* = \min(i, j)$ is used to describe the parameters associated with the linkage between the i^{th} and j^{th} rotator. Vectors $\boldsymbol{r}$ and $\boldsymbol{L}$ then represent the angular positon of the rotator and stretch of the linkage, respectively. Guided by experimental observations, we model the dissipation torque as a combination of linear viscous damping and Coulomb friction with viscous coefficient c_i and frictional torque $\boldsymbol{T}_{if}$,

$$\boldsymbol{T}_i = -c_i \dot{\boldsymbol{\theta}}_i - sgn(\theta_i) \boldsymbol{T}_{if} \tag{9}$$

Since we are interested in small-angle oscillations, we introduce a small parameter $\acute{U} \ll 1$ to scale the angular displacements, $\theta_i \to \acute{U}\theta_i$, and express the governing equations in a Taylor series with respect to U,

$$I_1 \ddot{\theta}_1 + \left(k_{g1}\theta_1 + k_{12}(\theta_1 + \theta_2) \right)\acute{U} + \left(\gamma_{12}^{+}(\theta_1 + \theta_2)^3 + \gamma_{12}^{-}(\theta_1 - \theta_2)^3 + \gamma_{g1}\theta_1^3 \right)\acute{U}^3 + O\left(\acute{U}^5\right)$$

$$+ c_1\dot{\theta}_1 + sgn(\theta_1) T_{1f} = 0 \tag{10}$$

$$I_2 \ddot{\theta}_2 + \left(k_{g2}\theta_2 + k_{12}(\theta_1 + \theta_2) + k_{23}(\theta_2 + \theta_3) \right)\acute{U}$$

$$+ \left(\gamma_{12}^{+}(\theta_1 + \theta_2)^3 + \gamma_{23}^{+}(\theta_2 + \theta_3)^3 + \gamma_{12}^{-}(\theta_2 - \theta_1)^3 + \gamma_{23}^{-}(\theta_2 - \theta_3)^3 + \gamma_{g2}\theta_2^3 \right)\acute{U}^3 + O\left(\acute{U}^5\right)$$

$$+ c_2\dot{\theta}_2 + sgn(\theta_2) T_{2f} = 0 \tag{11}$$

$$I_3 \ddot{\theta}_3 + \left(k_{g3}\theta_3 + k_{23}(\theta_2 + \theta_3) \right)\acute{U} + \left(\gamma_{23}^{+}(\theta_2 + \theta_3)^3 + \gamma_{23}^{-}(\theta_3 - \theta_2)^3 + \gamma_{g3}\theta_3^3 \right)\acute{U}^3 + O\left(\acute{U}^5\right)$$

$$+ c_3\dot{\theta}_3 + sgn(\theta_3) T_{3f} = 0 \tag{12}$$

where the linear stiffness k_{gi}, k_{ij}, and nonlinear stiffness γ_{ij}^{+}, γ_{ij}^{-} and γ_{gi} are functions of the system parameters – the Appendix provides complete expressions for each. Note that the linear stiffnesses k_{gi} and k_{ij} are both proportional to the pretension of the springs ($D_i - L_i$).

Eqs. (10)-(12) document that (i) the system only contains odd (hardening) nonlinearities, and (ii) its linear stiffness can be modified or eliminated by adjusting or removing the pretensions of the springs. In both linear and cubic terms, the restoring torque depends on the sum of angular displacement, $\theta_i + \theta_j$, unlike rectilinear counterparts which depend on displacement differences. In fact, this subtle difference results in a qualitative difference in the wave propagation problem in a periodic structure composed of such rotator structures. Please See Supplementary Material [40] for an extended discussion.

3 Experimental Results

Figure 3a depicts three 3D-printed rotators, each with radius 28.5mm, attached to low friction bearings affixed to a vibration isolation table. By varying the quantity of nuts and bolts attached to each rotator, an asymmetrical moment of inertia distribution can be introduced. In the designed experiment, from left to right, the rotators have inertia, 3.45×10^{-6},1.28×10^{-5}, and $3.16\times10^{-5}\ kgm^2$, respectively. As illustrated in Fig. 3b, the elastic linkage between two adjacent rotators consists of a weakly pre-tensioned short spring and two metal rings, which allows for axial extension and prevents spring bending. These elements have negligible mass compared to the three rotators and are all sufficiently lubricated. We perform a system identification study utilizing the *patternsearch* function in MATLAB, (detailed in Supplementary Material [40]) to accurately match the physical

experiment to our analytical model, which employs MATLAB's ODE45 function to numerically integrate the governing equations. We present the identified experimental parameters below.

Table 1. System parameter identification results.

	Rotator 1	Rotator 2	Rotator 3
Moment of Inertia I_i (kgm^2)	3.45×10^{-6}	1.28×10^{-5}	3.16×10^{-5}
Dissipation Coefficients c_i (Nms)	1.31×10^{-5}	8.7×10^{-6}	9.8×10^{-6}
Dissipation Coefficients T_{if} (Nm)	6.0×10^{-7}	3.18×10^{-6}	1.2×10^{-6}
	Linkage 1	Linkage 2	
Stiffness k_i (N/m)	870	670	
Un-deformed Length L_i (mm)	11.44	11.48	
Gap distance D_i (mm)	11.74	11.84	

We use an impact hammer to strike a rotator arm at either end of the chain using the same impulse level. The impacts are carefully applied at roughly the same distance from the center of the rotator such that the angular impulses are equal. We then use a laser Doppler vibrometer to capture the response at the other end of the chain. As such, we present the experimental non-reciprocal response in Figs. 2c-f, at an impulse level $P \approx 3.85 \pm 0.15\ Nms$, obtained from direct integration of experimental force responses, as depicted in the inscribed figures. Noteworthy, though the two impact excitations are not precisely the same (as shown in the inset figures), the impulse levels of two excitations are sufficiently close such that the contribution to reciprocity breaking from non-identical excitations is negligible compared to the nonlinear effects we present, as substantiated in Supplementary Note [40].

In Figs. 2c-d, the experimental responses show a high-degree of agreement with the superimposed numerical simulation results. We observe a large response at the left rotator when the impact excites the right rotator, compared to a smaller response at the right rotator when exciting the left

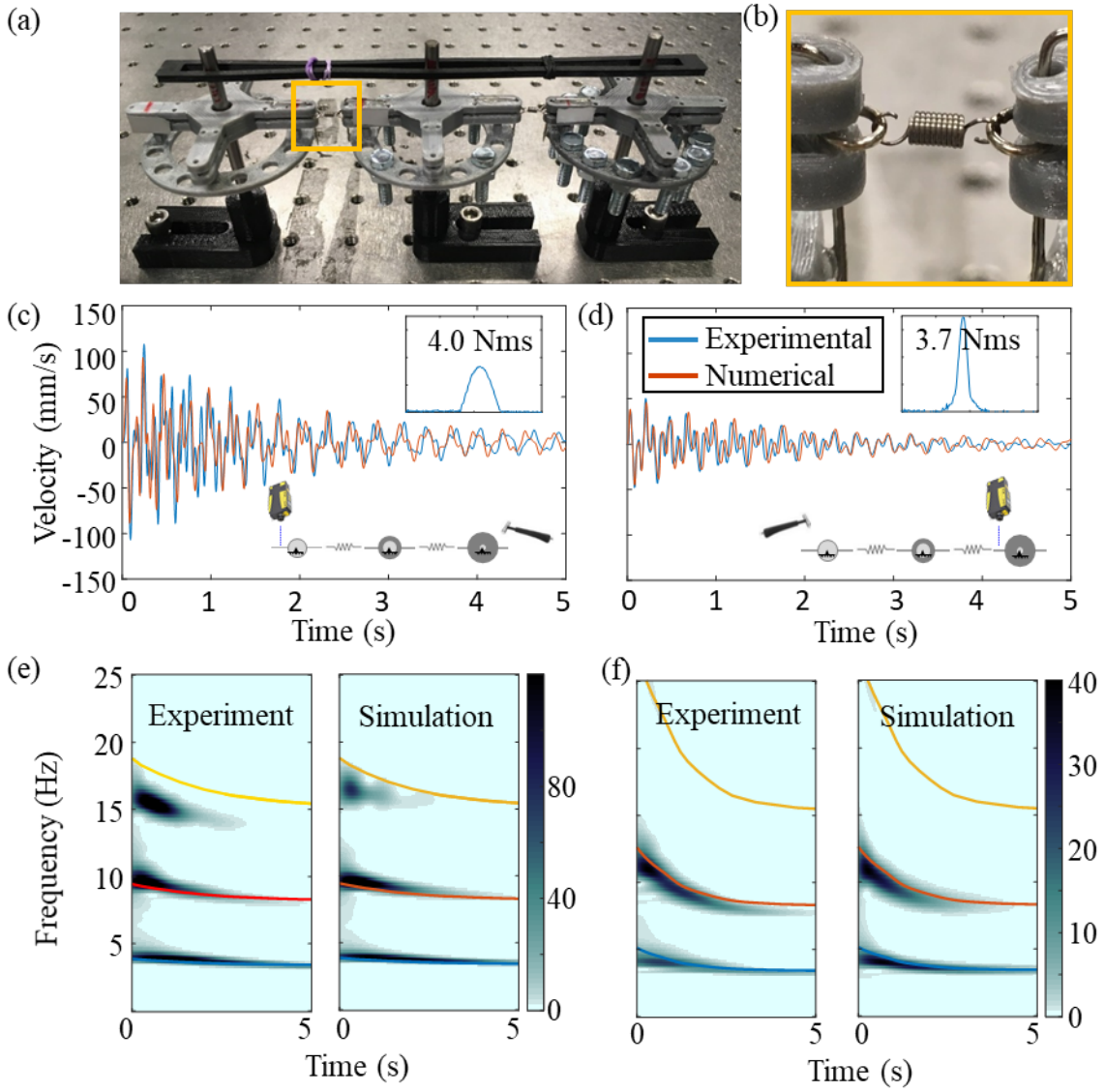

Figure 2: Experimental/numerical non-reciprocity results. (a) Experimental setup used in testing, (b) detailed view of the spring connection, (c) time response (numerical and experimental) of the small (left) rotator when excitation is applied on the right. The impact (force in N. vs. time in ms.) is documented in the top right corner, (d) time response (numerical and experimental) of the large (right) rotator, when the excitation is applied on the left. The impact is again plotted in the top right corner, (e) and (f) wavelet transformation (shaded) of the time responses shown in (c) and (d), superimposed by the nonlinear normal modes (solid lines) of the system.

rotator. A roughly 2:1 amplitude ratio appears in both experimental and numerical results. Results from a wavelet transformation performed on the experimental and numerical responses are displayed in Figs. 2e-f, respectively. The wavelet results clarify the strong non-reciprocity in the frequency domain. Three dominant harmonics in the left rotator response show considerable amplitude when the right rotator is excited, yet only two such harmonics appear in the right rotator response when the impulse is applied on the left.

4 Nonlinear Normal Mode (NNM) Analysis

In order to better illustrate the dynamics of the system and interpret the non-reciprocal phenomenon, we apply a nonlinear normal mode (NNM) analysis to the three degree-of-freedom geometrically nonlinear system. Similar to linear normal modes (LNM), NNMs depict periodic solutions of the nonlinear ODEs, yet in an energy-dependent framework. As defined by Shaw and Pierre in [41,42], a NNM is a two-dimensional invariant manifold in phase space, where an orbit starting on the manifold stays on the manifold for all time. At low energy limits, the NNM manifold is tangent to the corresponding LNM, which is represented by a plane in the phase space. Different from the displacement ratio in the linear mode shape concept, each NNM prescribes specific displacements for each degree of freedom, and hence a specific energy level for the entire system. We use the Newmark method and a continuation algorithm to numerically compute the NNMs, as detailed in [43-45], keeping only terms up to $O\left(U^{5}\right)$ in Eqs. (10)-(12). The energy-sensitive NNM can then be well illustrated in a frequency-energy plot accompanied with specific nonlinear mode shapes, which are the major focus of the following analysis.

In Fig. 3a, three NNM branches emerge, each of them exhibiting increasing frequency with increasing modal energy. To verify with experimental/numerical results, we compute the instantaneous energy of the system at each time, and then replace the energy axis of Figure 3a with time. The resultant plot is then superimposed on Figs. 2e-f, where we find a high degree of agreement between the frequency evolution and NNM trajectories. Note that the

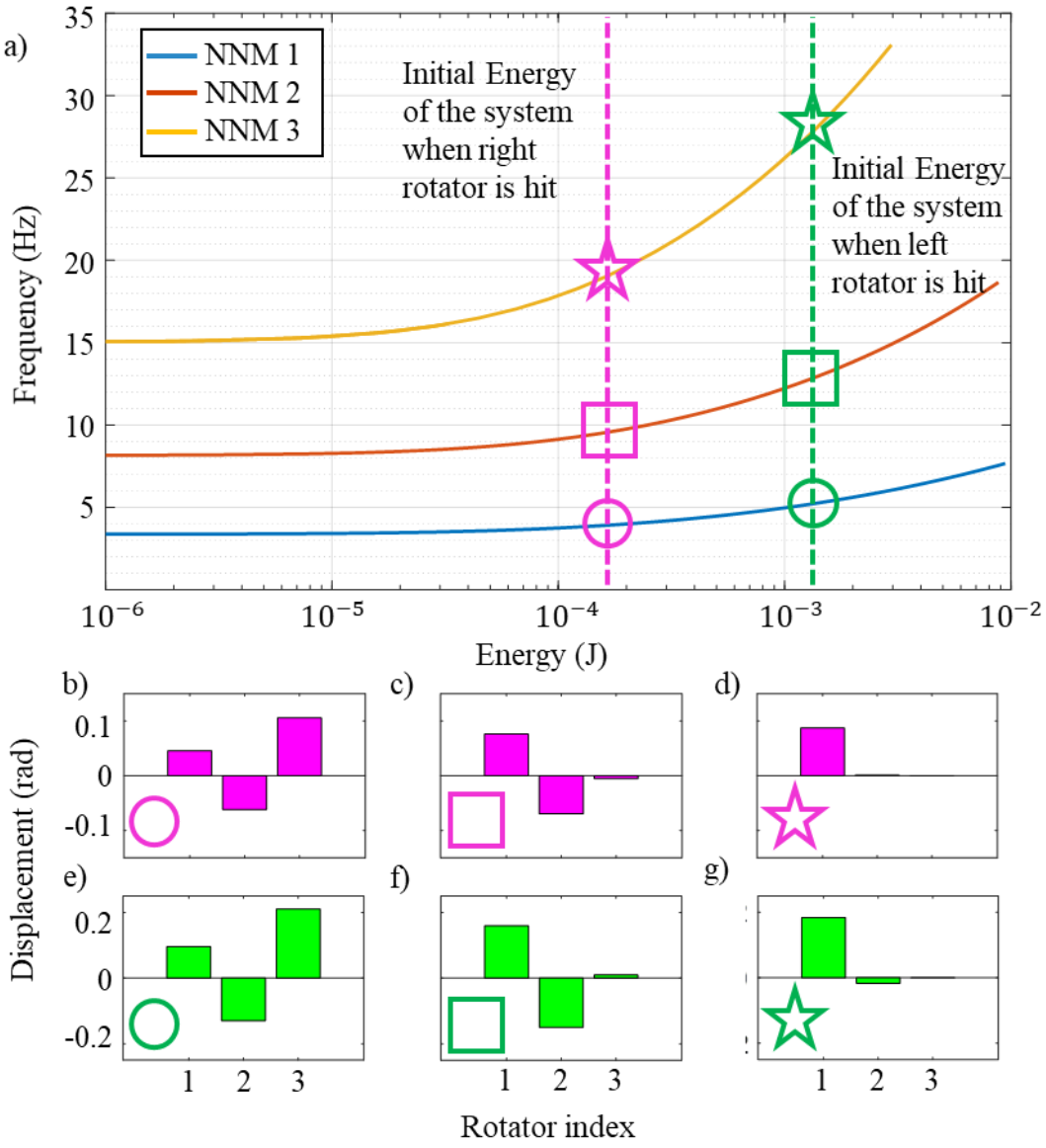

Figure 3: (a) Computed nonlinear normal modes (NNMs) of the system. Two vertical dashed lines indicate the energy level of the system when one rotator is excited. (b)-(g) Nonlinear mode shapes corresponding to the markers in (a). Rotator 1, 2 and 3 represents the small, medium and large rotator, respectively.

experimental/numerical frequency branches are expected to be lower than the NNM results, since the dynamics composed of multiple NNMs (in our case, three) must have a total energy no less than the energy of each composed NNM. Conversely, the energy of each NNM in the presented dynamics must be lower than the total energy of the system as captured in simulations/experiments. In a hardening nonlinear system, a lower energy leads to a lower frequency, as also illustrated in Fig. 3a.

The energy-dependent dynamics uncovered by the NNM analysis is key to understanding the non-reciprocal dynamics. In the studied system, due to the moment of inertia difference of the excited rotator, the same level of inputted impulse results in distinct initial energy ($E = P^2 / 2I_i$) inputted to the system. As indicated by the dashed lines in Fig. 3a, the excitation on the left rotator (small moment of inertia) results in a larger initial energy (green dashed line) than the energy (purple dashed line) resulting from excitation on the right rotator (large moment of inertia). From these starting energies, dissipation then drives the response frequency leftwards to the low energy regime in Fig. 3a. As such, the responses are associated with non-identical oscillation frequencies, which breaks reciprocity in the frequency domain, and matches the observations in Figs. 2e-f.

Moreover, the nonlinearity not only generates the aforementioned frequency variation, but also leads to different nonlinear mode shapes for each excitation event. Figures 3b-g illustrate the nonlinear normal mode shapes for each mode at two different energy levels (purple and green). Despite the difference in the amplitude of modal displacement (nonlinear normal modes are energy dependent, and cannot be normalized), the modes are fundamentally dissimilar at the given two energy levels. In the second mode (Figs. 3c and f), the modal displacement of the large rotator

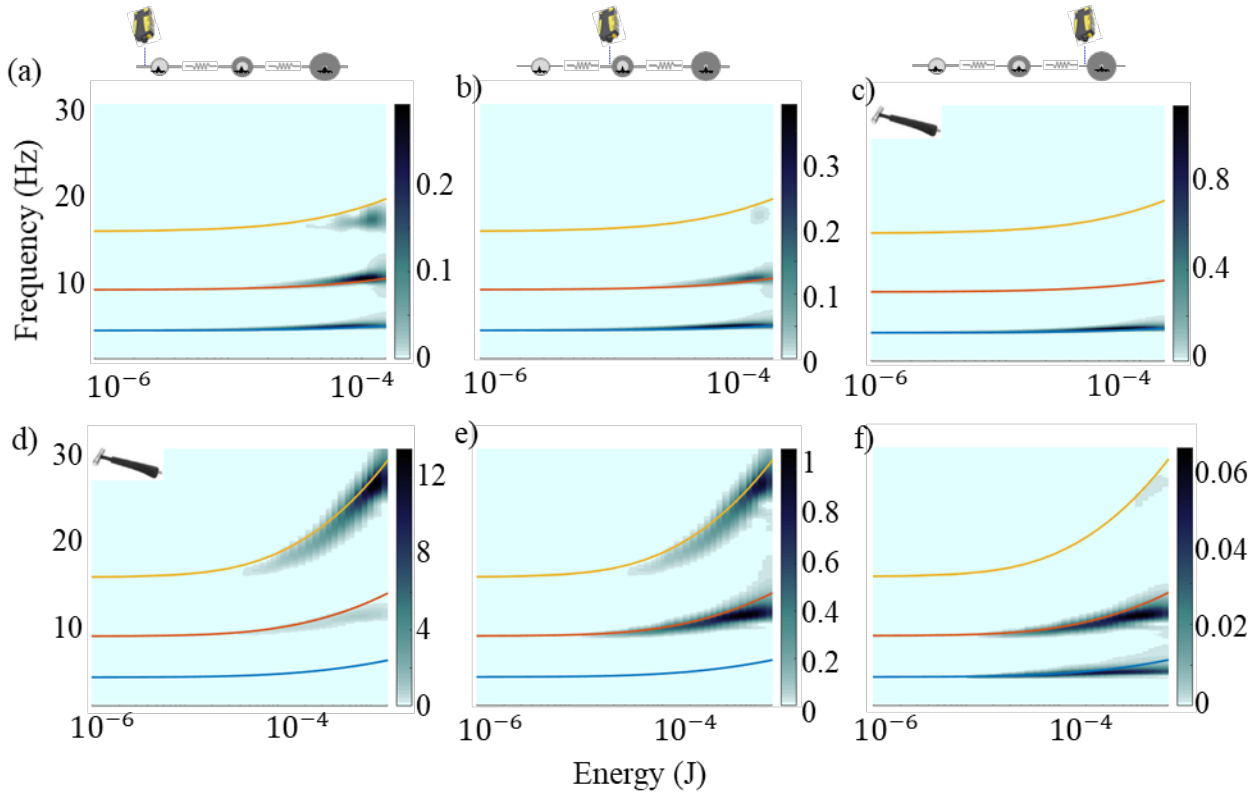

Figure 4: The wavelet response of the impulse excitation superimposed with NNM results. (a)-(c) The wavelet response for each rotator when the impulse applies on the large rotator. (d)-(f) The wavelet response for each rotator when the impulse applies on the small rotator. Each column represents corresponding rotator, e.g. the first column describes the response of the small rotator as indicated by the schematics on the top. The hammer symbol in (c) and (d) indicates the impulse excitation applies at this rotator.

(Rotator 3) is out-of-phase with respect to the small rotator (Rotator 1) at low energy, yet becomes in-phase with the small rotator at high energy. Similarly, in the third mode, the modal displacement of the medium rotator (Rotator 2) changes its sign at two energy levels as indicated in Figs. 3d, g.

In Fig. 4 we present the modal participation of these NNMs as predicted by the numerical model. We superimpose the NNMs on the wavelet results for each rotator under different excitation, whose horizontal axes are replaced by the instantaneous energy of the system (unlike Fig. 2 which uses time). The color of each frequency branch reveals the modal participation at this rotator. Note that the intensity of the frequencies vary from rotator to rotator, and thus the range of the color

bars are not chosen to be identical. Similar to LNMs, the participation of each NNM reacts to the initial conditions. When the impulse is applied to the large rotator, we observe in Fig. 4c that most of this rotator's response is dominated by the first NNM. As documented in Figs. 4a-b, the other two rotators exhibit response from all three NNMs, albeit it at lower amplitudes that observed in Fig. 4c. When the impulse is applied to the small inertia rotator, however, we observe in Fig. 4d a very large modal participation in the third NNM for this rotator, while the large inertia shows a correspondingly small participation in this NNM as shown in Fig. 4f. These results qualitatively match the mode shapes in Figs. 3b-g. In such a qualitative view, we have shown that, upon the same impulse excitation, as required by the reciprocity theorem, the response dynamics are distinct in both frequency and amplitude (mode shape).

Further, we show next that non-reciprocity still holds even if we seek an approximate solution of the system as a linear combination of the obtained NNMs, similar in spirit to the harmonic balance method. To this end, consider a combination of NNMs at the excitation energy level, with the energy-dependent frequency ω and mode shapes v provided in Table 2.

Table 2. Frequency and mode shapes for each nonlinear normal mode at the excited energy

	ω_1 (Hz)	ω_2 (Hz)	ω_3 (Hz)	$\boldsymbol{v}_1$	$\boldsymbol{v}_2$	$\boldsymbol{v}_3$
Large Inertia Excitation	3.88	9.50	19.00	$\begin{bmatrix} -0.046 \\ 0.062 \\ -0.106 \end{bmatrix}$	$\begin{bmatrix} -0.076 \\ 0.070 \\ -0.005 \end{bmatrix}$	$\begin{bmatrix} -0.087 \\ -0.001 \\ 0 \end{bmatrix}$
Small Inertia Excitation	5.22	12.84	27.86	$\begin{bmatrix} -0.096 \\ 0.130 \\ -0.210 \end{bmatrix}$	$\begin{bmatrix} -0.159 \\ 0.150 \\ -0.010 \end{bmatrix}$	$\begin{bmatrix} -0.184 \\ 0.017 \\ 0 \end{bmatrix}$

We seek an approximate solution in the modal form,

$$x = C_1\boldsymbol{v}_1 \sin\left(\omega_1 t + \phi_1\right) + C_2\boldsymbol{v}_2 \sin\left(\omega_2 t + \phi_2\right) + C_3\boldsymbol{v}_3 \sin\left(\omega_3 t + \phi_3\right), \tag{13}$$

where C_i and ϕ_i denote constants determined by the initial conditions,

$$\boldsymbol{x}(0)_{\boldsymbol{l}} = 0, \dot{\boldsymbol{x}}(0)_{\boldsymbol{l}} = \begin{Bmatrix} 0 \\ 0 \\ \dfrac{P r^*}{I_3} \end{Bmatrix} \tag{14}$$

$$\boldsymbol{x}(0)_{\boldsymbol{s}} = 0, \dot{\boldsymbol{x}}(0)_{\boldsymbol{s}} = \begin{Bmatrix} \dfrac{\mathrm{P\ r}^*}{I_1} \\ 0 \\ 0 \end{Bmatrix}. \tag{15}$$

In Eqs. (13)-(15) we have converted the impulse excitation P to into an equivalent initial velocity, $\frac{\mathrm{P\ r}^*}{I_i}$, with r^* being the distance between the excitation point to the center of the rotator, and subscripts $\boldsymbol{l}$ denotes the large inertia excitation and $\boldsymbol{s}$ on the small inertia excitation. Recall that the former initial condition results in a lower energy E_1 while the latter results in a higher energy E_2. After computing $C_1 \ldots C_3$ and $\phi_1 \ldots \phi_3$, we update Eq. (13) and present the receiving signal as

$$(x_1)_{\boldsymbol{l}} = 0.0603\sin(24.38t) - 0.0360\sin(59.69t) + 0.0057\sin(119.38t) \tag{16}$$

$$(x_3)_{\boldsymbol{s}} = 0.0084\sin(32.80t) - 0.0027\sin(80.68t) - 0.0003\sin(175.05t), \tag{17}$$

where $(x_1)_{\boldsymbol{l}}$ represents the response of the small rotator at large inertia excitation, and $(x_3)_{\boldsymbol{s}}$ the response of the large rotator under small inertia excitation. Clearly, reciprocity is broken, as these

two responses exhibit significantly different modal amplitudes and frequencies, unlike that recovered by a similar procedure for a linear system where the responses would be identical. We also observe that the response in Eq. (16) has larger modal amplitudes for each mode, and lower oscillating frequencies, as compared to the response in Eq. (17), which qualitatively matches the experimental results in Figs. 2c-f.

5 Concluding Remarks

In conclusion, we experimentally and numerically demonstrate non-reciprocal impulse response in an asymmetric in-plane rotator system, where tunable nonlinearity arises from pre-stretch of elastic linkages. We use a nonlinear normal mode analysis to capture the major dynamics of the system and find a high degree of agreement between theory and experiment. A further analysis reveals that the same level of impulses applied on rotators with differing moments of inertia induce differing initial energy, which contributes to non-identical oscillation frequency and dissimilar mode shapes, ultimately yielding non-reciprocal response.

The analysis of reciprocity-breaking, informed by a NNM analysis, should be applicable to a large class of nonlinear, non-reciprocal systems where identical impulses induce asymmetrical energy input. Because of the simplicity of the proposed mechanical system, the structure can be easily modified as a nonlinear attachment to control waves in a linear wave guide, or tuned as a shock isolator which protects targets from high energy impacts while maintaining the energy transmission in the opposite direction. Future work aims to extend the structure to 1D and 2D periodic lattices and study its dynamical response subject to harmonic excitations.

Acknowledgements

The authors would like to thank the National Science Foundation for partial support of this research under an Emerging Frontiers in Research and Innovation (EFRI) Grant, No. 1741565.

Appendix

Stiffness Expressions

The functional dependence of stiffness parameters appearing in Eqs. (10)-(12) are provided in Table A1.

Table A1. Stiffness expressions.

k_{g1}	$k_1 r\left(D_1 - L_1\right)$
k_{g2}	$k_1 r\left(D_1 - L_1\right) + k_2 r\left(D_2 - L_2\right)$
k_{g3}	$k_2 r\left(D_2 - L_2\right)$
k_{12}	$\dfrac{k_1 r^2\left(D_1 - L_1\right)}{D_1}$
k_{23}	$\dfrac{k_2 r^2\left(D_2 - L_2\right)}{D_2}$
γ_{g1}	$\dfrac{k_1 r}{3}\left(\dfrac{2r^2 L_1}{D_1^2} - r + \dfrac{2rL_1}{D_1} - \dfrac{D_1 - L_1}{2}\right)$
γ_{g2}	$\dfrac{k_1 r}{3}\left(\dfrac{2r^2 L_1}{D_1^2} - r + \dfrac{2rL_1}{D_1} - \dfrac{D_1 - L_1}{2}\right) + \dfrac{k_2 r}{3}\left(\dfrac{2r^2 L_2}{D_2^2} - r + \dfrac{2rL_2}{D_2} - \dfrac{D_2 - L_2}{2}\right)$
γ_{g3}	$\dfrac{k_2 r}{3}\left(\dfrac{2r^2 L_2}{D_2^2} - r + \dfrac{2rL_2}{D_2} - \dfrac{D_2 - L_2}{2}\right)$
γ_{12}^{+}	$\dfrac{k_1 r^2 L_1}{2D_1}\left(\dfrac{r^2}{D_1^2} + \dfrac{5r}{6D_1} + \dfrac{1}{6}\right)$
γ_{23}^{+}	$\dfrac{k_2 r^2 L_2}{2D_2}\left(\dfrac{r^2}{D_2^2} + \dfrac{5r}{6D_2} + \dfrac{1}{6}\right)$
γ_{12}^{-}	$\dfrac{k_1 r^2}{6}\left(1 - \dfrac{rL_1}{2D_1^2} - \dfrac{L_1}{2D_1}\right)$
γ_{23}^{-}	$\dfrac{k_2 r^2}{6}\left(1 - \dfrac{rL_2}{2D_2^2} - \dfrac{L_2}{2D_2}\right)$

References

[1] H. v. Helmholtz, Journal für die reine und angewandte Mathematik **57**, 1 (1860).
[2] J. Strutt, Proceedings of the London Mathematical Society **1**, 357 (1871).
[3] H. B. G. Casimir, Reviews of Modern Physics **17**, 343 (1945).
[4] A. F. Vakakis, O. V. Gendelman, L. A. Bergman, D. M. McFarland, G. Kerschen, and Y. S. Lee, *Nonlinear targeted energy transfer in mechanical and structural systems* (Springer Science & Business Media, 2008), Vol. 156.
[5] A. Darabi and M. J. Leamy, Nonlinear Dynamics **87**, 2127 (2017).
[6] K. J. Moore, J. Bunyan, S. Tawfick, O. V. Gendelman, S. Li, M. Leamy, and A. F. Vakakis, Physical Review E **97**, 012219 (2018).
[7] J. Li, X. Zhou, G. Huang, and G. Hu, Smart Materials and Structures **25**, 045013 (2016).
[8] C. Wang, S. Tawfick, and A. F. Vakakis, Physica D: Nonlinear Phenomena **402**, 132229 (2020).
[9] A. Darabi, L. Fang, A. Mojahed, M. D. Fronk, A. F. Vakakis, and M. J. Leamy, Physical Review B **99**, 214305 (2019).
[10] B. Liang, X. Guo, J. Tu, D. Zhang, and J. Cheng, Nature materials **9**, 989 (2010).
[11] B. Liang, B. Yuan, and J.-c. Cheng, Physical review letters **103**, 104301 (2009).
[12] R. Fleury, D. L. Sounas, C. F. Sieck, M. R. Haberman, and A. Alù, Science **343**, 516 (2014).
[13] Y. Chen, X. Li, H. Nassar, A. N. Norris, C. Daraio, and G. Huang, Physical Review Applied **11**, 064052 (2019).
[14] Z. Wu, Y. Zheng, and K. Wang, Physical Review E **97**, 022209 (2018).
[15] T. Devaux, A. Cebrecos, O. Richoux, V. Pagneux, and V. Tournat, Nature Communications **10**, 3292 (2019).
[16] Y. Li, C. Shen, Y. Xie, J. Li, W. Wang, S. A. Cummer, and Y. Jing, Physical review letters **119**, 035501 (2017).
[17] J. Bunyan, K. J. Moore, A. Mojahed, M. D. Fronk, M. Leamy, S. Tawfick, and A. F. Vakakis, Physical Review E **97**, 052211 (2018).
[18] G. Trainiti, Y. Xia, J. Marconi, G. Cazzulani, A. Erturk, and M. Ruzzene, Physical review letters **122**, 124301 (2019).
[19] L. Fang, A. Darabi, A. Mojahed, A. F. Vakakis, and M. J. Leamy, Nonlinear Dynamics, 1 (2020).
[20] S. H. Mousavi, A. B. Khanikaev, and Z. Wang, Nature Communications **6**, 8682 (2015).
[21] C. P. Wiederhold, D. L. Sounas, and A. Alù, The Journal of the Acoustical Society of America **146**, 802 (2019).
[22] H. Nassar, X. Xu, A. Norris, and G. Huang, Journal of the Mechanics and Physics of Solids **101**, 10 (2017).
[23] G. Trainiti and M. Ruzzene, New Journal of Physics **18**, 083047 (2016).
[24] J. Li, C. Shen, X. Zhu, Y. Xie, and S. A. Cummer, Physical Review B **99**, 144311 (2019).
[25] X. Zhu, J. Li, C. Shen, X. Peng, A. Song, L. Li, and S. A. Cummer, Applied Physics Letters **116**, 034101 (2020).
[26] L. Quan, D. L. Sounas, and A. Alù, Physical review letters **123**, 064301 (2019).
[27] B.-I. Popa and S. A. Cummer, Nature communications **5**, 3398 (2014).
[28] N. Boechler, G. Theocharis, and C. Daraio, Nature materials **10**, 665 (2011).
[29] E. Rivet, A. Brandstötter, K. G. Makris, H. Lissek, S. Rotter, and R. Fleury, Nature Physics **14**, 942 (2018).
[30] H. Nassar, B. Yousefzadeh, R. Fleury, M. Ruzzene, A. Alù, C. Daraio, A. N. Norris, G. Huang, and M. R. Haberman, Nature Reviews Materials, 1 (2020).
[31] C. Coulais, D. Sounas, and A. Alù, Nature **542**, 461 (2017).

[32] Z. Lu and A. N. Norris, Journal of Vibration and Acoustics **142** (2020).
[33] A. Mojahed and A. F. Vakakis, Nonlinear Dynamics **99**, 643 (2020).
[34] K. L. Manktelow, M. J. Leamy, and M. Ruzzene, Wave Motion **51**, 886 (2014).
[35] A. Darabi and M. Leamy, NONLINEAR VIBRATIONS, LOCALIZATION AND ENERGY TRANSFER, 58.
[36] A. Blanchard, T. P. Sapsis, and A. F. Vakakis, Journal of Sound and Vibration **412**, 326 (2018).
[37] O. Gendelman, V. Zolotarevskiy, A. Savin, L. Bergman, and A. Vakakis, Physical Review E **93**, 032216 (2016).
[38] O. Rudenko and E. Solodov, Acoustical Physics **57**, 51 (2011).
[39] Z. Zhang, L. I. Manevitch, V. Smirnov, L. A. Bergman, and A. F. Vakakis, Journal of the Mechanics and Physics of Solids **110**, 1 (2018).
[40] See Supplementary at [URL] for external discussion on peridoic structure, experimental parameter identification and effects of imperfect excitation.
[41] S. Shaw and C. Pierre, (1991).
[42] S. W. Shaw and C. Pierre, Journal of sound and vibration **164**, 85 (1993).
[43] G. Kerschen, M. Peeters, J.-C. Golinval, and A. F. Vakakis, Mechanical Systems and Signal Processing **23**, 170 (2009).
[44] M. Peeters, R. Viguié, G. Sérandour, G. Kerschen, and J.-C. Golinval, Mechanical systems and signal processing **23**, 195 (2009).
[45] J. C. Slater, Nonlinear dynamics **10**, 19 (1996).